J. Fluid Mech. (2008), *vol.* 610, *pp.* 217–247.
doi:10.1017/S0022112008002383 Printed in the United Kingdom

Beating of a circular cylinder mounted as an inverted pendulum

A. VOORHEES[1], P. DONG[2], P. ATSAVAPRANEE[3], H. BENAROYA[2] AND T. WEI[4]

[1]Siemens Medical Solutions USA, Inc., Phildaelphia, PA 19104, USA
[2]Department of Mechanical and Aerospace Engineering, Rutgers University, Piscataway, NJ 08854-8058, USA
[3]Naval Surface Warfare Center, West Bethesda, MD 21218, USA
[4]Department of Mechanical, Aerospace and Nuclear Engineering, Rensselaer Polytechnic Institute, Troy, NY 12180-3590, USA

(Received 22 August 2003 and in revised form 19 February 2008)

This paper contains temporally and spatially resolved flow visualization and DPIV measurements characterizing the frequency–amplitude response and three-dimensional vortex structure of a circular cylinder mounted like an inverted pendulum. Two circular cylinders were examined in this investigation. Both were 2.54 cm in diameter and $\sim$140 cm long with low mass ratios, $m^* = 0.65$ and 1.90, and mass–damping ratios, $m^*\zeta = 0.038$ and 0.103, respectively. Frequency–amplitude response analysis was done with the lighter cylinder while detailed wake structure visualization and measurements were done using the slightly higher-mass-ratio cylinder. Experiments were conducted over the Reynolds number range $1900 \leqslant Re \leqslant 6800$ corresponding to a reduced velocity range of $3.7 \leqslant U^* \leqslant 9.6$. Detailed examination of the upper branch of the synchronization regime permitted, for the first time, the identification of short-time deviations in cylinder oscillation and vortex-shedding frequencies that give rise to beating behaviour. That is, while long-time averages of cylinder oscillation and vortex-shedding frequencies are identical, i.e. synchronized, it is shown that there is a slight mismatch between these frequencies over much shorter periods when the cylinder exhibits quasi-periodic beating. Data are also presented which show that vortex strength is also modulated from one cylinder oscillation to the next. Physical arguments are presented to explain both the origins of beating as well as why the quasi-periodicity of the beating envelopes becomes irregular; it is believed that this result may be generalized to a broader class of fluid–structure interactions. In addition, observations of strong vertical flows associated with the Kármán vortices developing 2–3 diameters downstream of the cylinder are presented. It is hypothesized that these three-dimensionalities result from both the inverted pendulum motion as well as free-surface effects.

1. Introduction

1.1. *Frequency–amplitude response of an inverted pendulum*

Vortex-induced-vibrations (VIV) of elastically mounted cylinders, i.e. cylinders constrained at both ends by springs which oscillate in the cross-stream direction under the influence of their vortex shedding, is a dynamically rich field of study. Under the right conditions, Kármán vortices shed from the cylinder induce fluctuating lift forces

which excite transverse oscillations. When VIV occurs, the vortex shedding frequency, i.e. repeatable vortex patterns, is approximately equal to the oscillation frequency of the cylinder; this has been referred to as *synchronization* and the range of flow speeds for which this occurs is called the *synchronization regime*. For extensive reviews, see Bearman (1984), Chen (1987), and Williamson (1996*a*).

Frequency and amplitude response characteristics of elastically mounted cylinders have been well documented. There are two main response types which depend on a mass–damping parameter, $m^*\zeta$, where m^* is the ratio of cylinder mass to the mass of the fluid displaced by the cylinder and ζ is the damping ratio of the structure. Cylinders with high $m^*\zeta$ are characterized by an amplitude response plot containing two branches; this is known as the 'Feng-type' response. The amplitude response of cylinders with low $m^*\zeta$ exhibit three distinct branches. For both low and high mass–damping, the lower branch of the amplitude response is characterized by cylinder oscillations at a single frequency and constant amplitude over a range of flow speeds. This is known as the classical 'lock-in' regime. For high mass ratios, m^*, however, the normalized frequency, f^*, i.e. the oscillation frequency divided by the natural frequency of the cylinder in water, is approximately equal to unity. For low m^* it has been shown that $f^* > 1.0$. See Khalak & Williamson (1999) for a complete discussion of these parameters.

In this study, VIV associated with vertically mounted, rigid, hollow, low-mass-ratio circular cylinders were examined. Unlike the two-dimensional elastically mounted cylinder, however, the cylinders in this study were mounted at the bottom end with a flexible pin with motion constrained to the cross-stream direction only. Frequency and amplitude response characteristics of the cylinders will be shown to be virtually identical to those for elastically mounted cylinders. Following the conventions chosen by Khalak & Williamson (1999), two distinct branches were observed. The initial excitation or upper branch, $3.8 < U^* < 7.0$, where reduced velocity, $U^* = U/f_n D$, is defined in the conventional way, is characterized by vortex-shedding frequencies different from $S = 0.21$. In addition, VIV is characterized by strong energetic vortices shed very close to the cylinder and by a beating behaviour of the cylinder oscillations. This has also been referred to as *resonant synchronization*.

The lower branch, occurring for $7.0 \leqslant U^* \leqslant 9.2$, is characterized by oscillation amplitudes and frequencies which do not vary with U^*. In this lock-in regime, cylinder oscillation frequency and amplitude remain constant over a wide range of flow speeds. Flow visualization studies presented in Atsavapranee, Benaroya & Wei (1999) and Voorhees (2002) indicated that in the classic lock-in regime, vortex shedding appeared rather disorganized in comparison to the resonant synchronization regime. This may be interpreted as the cylinder modulating the flow so that 'just enough' energy was transferred from fluid to structure to maintain a fixed amplitude oscillation at the natural frequency. At the end of this regime, the cylinder no longer vibrates in response to vortex shedding until, of course, the second harmonic of the cylinder natural frequency is approached.

1.2. *Three-dimensionality in the wakes of oscillating cylinders*

Even when the angle of oscillation is small, as considered by Atsavapranee *et al.* (1999), and subsequently by Dong (2002) and Voorhees (2002), the local Kármán vortex strength increases as the local oscillation amplitude grows with increasing distance from the fixed end. Variations in vortex strength, in turn, lead to axial pressure gradients along the Kármán vortices giving rise to axial flows away from the fixed end. This behaviour was observed for a cylinder mounted as an inverted

pendulum with a maximum deflection angle of only 1.5°. For the present case, strong vertical (i.e. axial) flows were observed even though the vertical displacement of any point on the cylinder was <3 % of horizontal displacement. When the structure is partially submerged in a liquid flow and pierces the free surface, the nature of the axial flows becomes quite complex. It is not clear what impact this three-dimensionality has on the modelling of small-amplitude VIV. Of particular interest to this study is the reduced-order analytical modelling effort described in Benaroya & Wei (2000), Dong (2002) and Dong, Benaroya & Wei (2004). The second focus of this paper, then, is the existence and importance of large-scale three-dimensionality in the wake of a freely oscillating, surface-piercing cylinder.

Three-dimensionality in the wakes of stationary and elastically mounted cylinders has received a great deal of attention over the last twenty years, though the existence of such flows has been noted for over half a century. In virtually all cylinder wakes, small-scale three-dimensionality in nominally two-dimensional wakes inevitably develops with increasing Reynolds number; see, for example Tombazis & Bearman (1997). Williamson (1996*b*) carefully documented the onset of small-scale three-dimensionality in cylinder wakes. He reported that transition occurs for $190 \leqslant Re \leqslant 250$ through the amplification and growth of spanwise instabilities. For $Re > 1000$, Williamson (1996*a*) notes that three-dimensional structures develop which scale both on the separated shear layers as well as on the Kármán vortices. For $Re > 1200$, Wei & Smith (1986) reported that small-scale spanwise vortices, originating in the separated cylinder boundary layers, develop spanwise waviness and realign in the stream direction.

The three-dimensionalities identified in the preceding paragraph are generally a natural part of the transition to turbulence of cylinder wakes. That is, they do not typically affect the mean two-dimensional wake structure. There are, however, large-scale three-dimensional phenomena, such as oblique vortex shedding, vortex dislocations, and cellular shedding, which are a clear departure from two-dimensionality on the mean. For more details, see Tombazis & Bearman (1997).

There are several investigations with modified cylinder geometries that have explored controlling such large-scale three-dimensionalities. Stationary tapered cylinders and cones have been studied by Gaster (1969, 1971). Free or forced vibrations of such structures were experimentally examined by Techet, Hover & Triantafyllou (1998) and Hover, Techet & Triantafyllou (1998). At low Re, Gaster (1969, 1971) found that vortex shedding from a slightly tapered cylinder or cone occurred at frequencies which varied (with local diameter) along the span and could lead to cellular shedding. At higher Re, forced oscillation of a tapered cylinder was investigated by Techet *et al.* (1998) using flow visualization. In addition to observing continuous Kármán vortices along the span, a split in vortex shedding was also observed at certain flow speeds. This split was characterized by two modes of shedding located at different spanwise positions. This so-called hybrid mode was found to be periodic whereas vortex dislocations, in general, were not. In a parallel study, Hover *et al.* (1998) investigated uniform and tapered cylinders in free and forced vibration. By measuring lift forces generated at each end, it was found that the tapered cylinder experienced smoother transitions through the various flow regimes. In none of the tapered cylinder experiments were axial flows observed.

There are two recent investigations, Fujarra *et al.* (2001) and Kittagawa, Fujono & Kimura (1999), in which cylinders were pinned at one end and free at the other. Fujarra *et al.* (2001) used a flexible cantilever in water over an Re range from 1000 to 2500. The stiffness orientation in the cantilever primarily allowed transverse oscillations over the entire synchronization regime. (Streamwise oscillations were noted at flow

speeds beyond synchronization.) The cylinder had a low mass ratio, $m^* = 1.3$, and relatively high mass–damping, $m^*\zeta = 0.185$. The amplitude and frequency response had two branches and the average f^* during lock-in was 1.3. Kittagawa *et al.* (1999) examined a rigid cantilever mounted using a leaf spring. Experiments were conducted in a wind tunnel at high *Re*. In addition to VIV, the authors noted an end-cell-induced vibration, which was caused by a vortex generated at the free end of the cylinder. It should be noted that flow visualizations were not performed in either cantilever study and, thus, spanwise flows in the wake of the cylinder could not be observed.

A common observation from a variety of free-surface turbulence investigations is that a free surface causes lateral spreading of near-surface turbulence and that turbulence interactions with a free surface are anisotropic. Logory, Hirsa & Anthony (1996) investigated the turbulent wake of a flat plate and observed that the near-surface wake width was found to double compared to the wake at depth. In addition, wake three-dimensionality was observed to markedly increase near the free surface. Grega *et al.* (1995) investigated turbulence in a 'mixed boundary corner' formed by a solid wall and free surface and observed that free-surface currents effectively thicken the boundary layer at the free surface. Walker Leighton & Garza-Rios (1996) conducted a numerical simulation of initially homogeneous and isotropic turbulence near a free surface and examined anisotropy approaching the free surface. They determined that dissipation became zero and mean pressure increased on approaching the free surface. Hsu *et al.* (2000) experimentally confirmed anisotropy of the dissipation in the mixed boundary corner. Warncke-Lang & Gharib (2000) examined free-surfac effects in the wake of a stationary cylinder for both clean and contaminated surfaces. They found that surfactants alter surface shear stress causing otherwise surface-normal Kármán vortices to reorient themselves in a surface parallel direction.

1.3. *Objectives*

Figure 1 contains two 360 s time traces of instantaneous cylinder deflection. The non-dimensional ordinate, $y/D = 0$, is centred on the cylinder rest position. These measurements were obtained using the signal from a Banner Omni-beam OASBD analog photoelectric sensor sampled at 100 Hz. If one looks at short segments of the traces, one can immediately see a richness in the oscillations that is ordinarily masked by averaging. In particular, one can clearly see irregularities in oscillation amplitude; for different parts of the traces, the cylinder appears to undergo quasi-periodic beating. Four examples of quasi-periodic beating have been identified in figure 1 by dotted rectangular boxes. After a few beat periods, however, the amplitude becomes either irregular or even constant for several more cycles. Examples of regions where the amplitude remains approximately constant have been identified in figure 1 using ovals.

While frequency–amplitude response plots are extremely helpful in characterizing different oscillation regimes, understanding and modelling the irregular oscillations highlighted in figure 1 is problematic. Indeed, long-time-averaged frequency and amplitude response data, shown in § 3, indicate that the cylinder oscillation frequency and vortex shedding frequency are identical. This leads to what will be shown as the incorrect conclusion that beating must be the result of phase shifts between the two frequencies. The critical new element of this study is the ability to conditionally sample fluid–structure interactions during quasi-periodic beating. The results of this analysis show that *frequency variations* play a key role in this phenomenon.

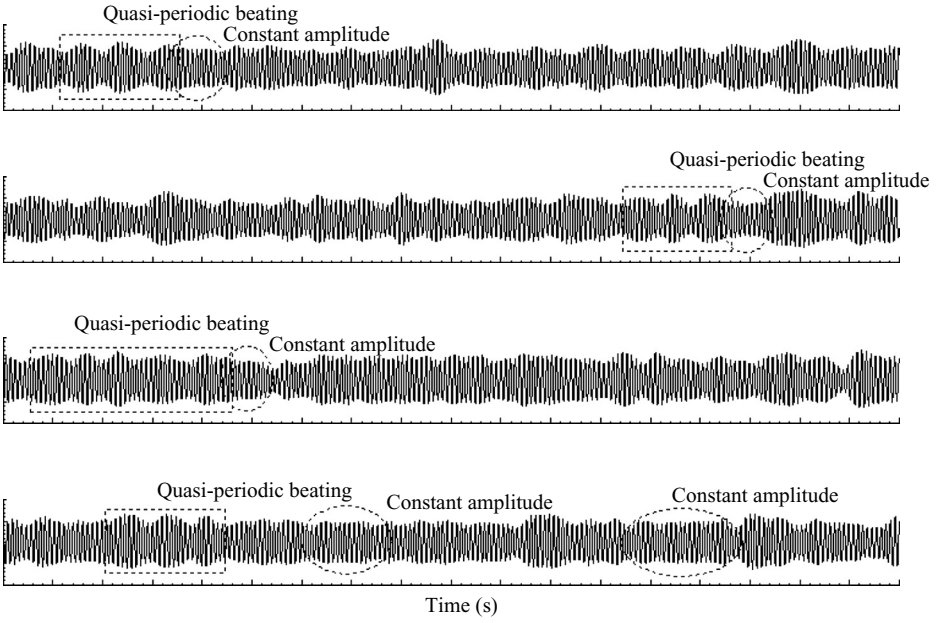

FIGURE 1. Two three-minute time traces showing instantaneous cylinder position *vs.* time for the cylinder undergoing vortex-induced-vibrations in the upper branch or synchronization regime. Note the irregularity of the amplitude modulations. Examples of quasi-periodic beating and constant amplitude are indicated.

This paper builds on earlier work by, e.g. Benaroya & Wei (2000), Dong (2002) and Dong *et al.* (2004), focused on developing reduced-order analytical models to describe quasi-periodic beating like that indicated in figure 1. Data from those studies revealed new insights into the coupling between vortex shedding and cylinder oscillations in the upper branch of the frequency-amplitude response plots. These insights will be further developed in this paper.

The second focus of this investigation is on understanding the nature of axial flows in the wake of a surface-piercing, rigid circular cylinder mounted as an inverted pendulum. While one can nominally treat this problem as an elastically mounted cylinder, even for the very small angular deflections of the leaf spring, there was evidence of three-dimensionality in the flow. In particular, early flow visualization studies indicated that dye injected into the wake at the cylinder mid-height would frequently move to or from the free-surface in very energetic ways. One could quickly reason that the upflows were the result of axial flows set up by vorticity gradients in the Kármán vortices. As one moves up toward the free surface, away from the pinned end, the cylinder amplitude increases. Consequently, one would expect the local vorticity in the Kármán vortex to also increase approaching the free-surface. This, in turn, would result in a pumping of fluid up the axes of the Kármán vortices up toward the free-surface.

The surprising observation was that there were also numerous instances where the axial flows were *down* away from the free-surface. Was this a free-surface effect? Or were there additional mechanisms at work. In the light of the irregularities in the cylinder oscillation amplitudes, the second focus of this paper is the question

of whether or not there is a relationship between the beating phenomena and axial flows.

1.4. *A note on coordinates*

Experiments and results are presented relative to a right-hand Cartesian coordinate system whose origin is defined by the axis of the cylinder at rest, and the free-surface. The x-axis corresponds to the mean stream direction; the y-direction is cross-stream and parallel to the free surface; and the z-axis is aligned opposite to gravity, i.e. vertically upward from the free-surface. In this manner, all distances below the surface are negative.

2. Experimental apparatus and methodologies

2.1. *Flow facility*

Experiments were conducted in the free-surface water tunnel described in Smith (1992) and Grega *et al.* (1995). The facility consists of an upstream end tank and settling chamber, contraction, test section, downstream end tank, and two pumps. The test section is 610 cm long, 122 cm deep, and 57.2 cm wide. The walls and floor are glass, allowing maximum optical access. The maximum flow rate is 1500 $\mathrm{l\,min^{-1}}$, corresponding to a free-stream speed of $\sim$30 $\mathrm{cm\,s^{-1}}$ when the test section is full. The free-stream velocity was found to be uniform to within $\pm$2% across the cross-section and turbulence intensities are less than 0.1% of the free-stream speed.

Under steady-state operation, the free-surface in the test section was effectively free of contaminants. This is because the rate at which surfactant diffuses to the free-surface is much slower than the rate at which water passes through the test section. Proof of a clean free-surface in the test section is the existence of a *Re*ynolds ridge located 20–50 cm upstream of the exit. For further details, see Grega *et al.* (1995).

2.2. *Cylinder overviews*

The results presented in this paper are a combination of two experiments with two similar, but different, circular cylinders. The primary difference between cylinders was construction material and, hence, mass ratio. One cylinder was used primarily for the frequency and amplitude response studies while the second cylinder was used to study three-dimensionality in the near wake.

2.2.1. *The lower mass ratio ($m^* = 0.65$) cylinder for frequency/amplitude response*

The first cylinder was constructed from a 141 cm length of thin-walled acrylic tube, 2.54 cm in diameter. Unlike a two-dimensional elastically mounted cylinder, however, the cylinder in this study was mounted on the test section floor of a large free-surface water tunnel by a 0.32 cm diameter stainless-steel pin. The top, free, end of the cylinder protruded through the free surface and was fitted with a cart assembly. The cart consisted of a block of PVC into which two ball bearings were mounted on the downstream face. These bearings rolled along an oiled polished steel plate mounted on a rigid bar spanning the water tunnel test section. In this manner, the cylinder was constrained to freely oscillate as an inverted pendulum only in the cross-stream plane. For details of the experiment, see Dong (2002) or Dong *et al.* (2004). An assembly drawing of the structure is shown in figure 2. Note that the mass of the cart with its bearings (not shown in figure 2) was included in the cylinder mass ratio.

The mass ratio, m^*, of the cylinder (including the mass of the cart) was 0.65 and the cylinder damping ratio, ζ, was 0.058; the mass–damping parameter, then, was

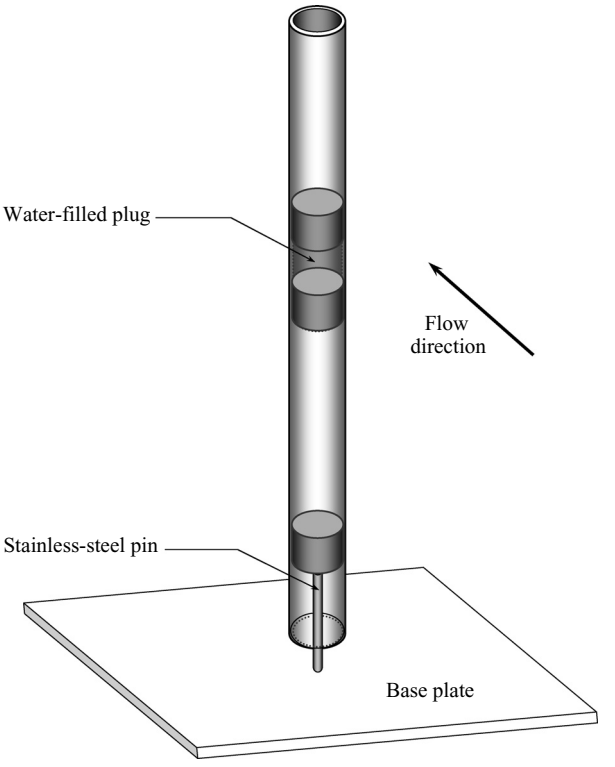

FIGURE 2. Schematic drawing of the thin-walled cylinder mounted on a base plate as an inverted pendulum using a stainless-steel pin. The cylinder was 141 cm long and 2.54 cm in diameter. (The drawing is not to scale.) Drawing includes the water filled plug at the mid-height used for passage of the laser sheet. The restraining cart permitting cross-stream motions only is not shown.

0.038. The structure's natural frequency, f_n, was 0.83 Hz in air and 0.77 Hz in water. The total moment of inertia for the entire cylinder assembly, I_0, was 0.40 kg m^2 and its stiffness, k_T was 11.0 N m rad^{-1}. Note that the maximum angular deflection, θ_{max}, was only 1.5°. It will be shown later that Kármán vortices remain continuous along the entire length of the cylinder, and that three-dimensional effects developed approximately three diameters downstream of the cylinder and are strongest at the free-surface.

2.2.2. *The higher mass ratio ($m^* = 1.90$) cylinder for three-dimensional flows*

The second cylinder used in this investigation was constructed using four lengths of thin-walled anodized aluminium tube rigidly connected by machined aluminium plugs, a stainless-steel leaf spring, base plate, and guiding cart. Each tube section was 26.7 cm long with 0.04 cm wall thickness. The plugs were 10.2 cm long with centres bored to permit passage of two 0.48 cm diameter dye injection tubes. One plug was specially manufactured with two 2.54 cm long $\times$ 0.10 cm wide dye injection slots aligned in the axial direction and spaced 60° apart. The other two were 'dummies' whose masses were made to match that of the injection plug. In this manner, the dye injection plug could be interchanged with either dummy plug, allowing flow visualization at different positions along the cylinder. Two o-rings were used both the ends of each plug to ensure rigidity of the cylinder assembly and to keep water from

leaking into the cylinder. The overall length and diameter of this cylinder was 142 cm and 2.54 cm, respectively.

The cylinder was mounted on a 1.27 cm thick base plate on the test section floor using a stainless-steel leaf spring. By aligning the spring in the flow direction, VIV was restricted to the transverse direction. The overall spring dimensions were 5.08 cm high, 2.54 cm long (in the stream direction), and 0.10 cm thick. The spring was clamped at both ends, thereby keeping the effective length to 2.54 cm. For small deflections, the leaf spring is assumed to act as a linear torsional spring with a spring constant, $\boldsymbol{k}$, of 38.8 N m rad^{-1}. The free end of the cylinder extended through the free-surface and was fitted with a guiding cart to further restrict cylinder oscillations to the transverse direction. The cart described in § 2.2.1 and shown in figure 2 was used on this cylinder as well. The mass ratio for this cylinder was 1.90. The natural frequency of the structure in water, f_n, was 1.09 s^{-1}. The ratio of mechanical to critical damping, ζ, was 0.054, and the mass–damping parameter, $m^*\zeta$, was 0.103. For the flow conditions studied in the investigation, the maximum VIV amplitude at the free end of the cylinder was approximately one cylinder diameter. This corresponds to a 1.5° maximum deflection angle.

2.3. *Cylinder position measurements*

Records of instantaneous cylinder position for either cylinder were measured using a Banner Omni-beam OASBD analog photoelectric sensor. The sensor operated on the principle of measuring the reflected intensity of an 880 nm infrared source beam. A small white reflecting surface was attached to the top of the cylinder to improve signal quality. Output from the position sensor was transferred to a PC through a 12-bit analog to digital A/D board. Cylinder position data were captured at 300 Hz, twenty times faster than the digital particle image velocimetry (DPIV) sampling rate. This ensured clean accurate position information each time flow data were acquired.

2.4. *Flow visualization*

Two-colour LIF and food colour flow visualization studies were conducted as part of this investigation. For both techniques, dye was injected through the two dye injection slots described in § 2.2. The dye injection slots were $\pm 30°$ on either side of the mean forward stagnation line of the cylinder at rest. For the laser-induced fluorescence (LIF) experiments, fluorescein (green) and rhodamine (red-orange) dyes were used. Flow was illuminated using a Coherent Innova 70-5 argon-ion laser.

Red and blue food colour was also used to mark the flow. For those studies, the water tunnel was back lit using a floodlamp directed through a diffuse surface. All visualizations were recorded with a Sony Professional 3-CCD camera on S-VHS videotape.

2.5. *The DPIV measurement system*

An in-house DPIV system was used to obtain velocity and vorticity measurements from the flow field. Details may be found in Hsu (2000). Flow was illuminated using a dual head Nd:YAG laser (New Wave Gemini PIV 120-15) which produced two laser pulses at 1/15 s intervals with output energies of 120 mJ per pulse. Timing was controlled by a Stanford Research Systems DG535 digital delay/pulse generator operating at 15 Hz. A Kodak Megaplus ES 1.0 digital video camera with 1008 × 1018 pixel resolution was used to capture video records of seeded flow. The camera output was connected to an Imaging Technology IC-PCI image-capture board located on a 300 MHz Pentium PC. This permitted capture of 450 consecutive video frames, i.e. 225 DPIV vector fields, corresponding to ~15 s temporally resolved records of the

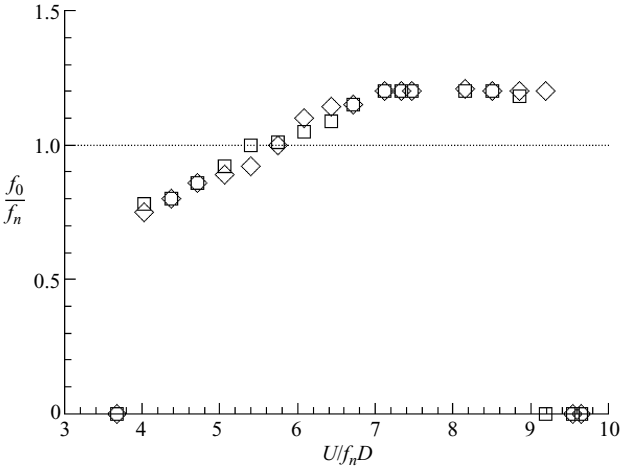

FIGURE 3. Dimensionless cylinder oscillation frequency, f_o/f_n *vs.* reduced velocity, U/f_nD. Squares denote measurements taken for incrementally increasing speeds while diamonds indicate data taken while decreasing through the speed range.

flow. Flow was seeded using 13 μm silver-coated hollow glass spheres with specific gravity of 1.6.

For measurements in (x, y)-planes, horizontal laser light sheets were deflected upstream using a front surface mirror mounted inside the test section at 45° to the flow. The video camera was placed under the test section looking upward, normal to the laser sheet. Measurements were also made in cross stream, (y, z)-planes. For these studies, vertical laser sheets were passed directly through the test section sidewalls and the 45° mirror in the test section was used to reflect the end-view out to the video camera.

Regardless of measurement plane, the camera output was connected to an Imaging Technology IC-PCI image-capture board located on a 300 MHz Pentium PC. This permitted capture of 450 consecutive video frames, i.e. 225 DPIV vector fields, corresponding to 22.5 s temporally resolved records of the flow.

DPIV vector fields were computed using an in-house DPIV software package featuring a two-step correlation process. Large interrogation windows were first used to obtain a 'coarse' particle displacement field. Displacements computed in the coarse correlation stage were then used as input to a 'fine' correlation stage, in which smaller interrogation windows were appropriately displaced to obtain an accurate 'fine' displacement field. Four times over-sampling was used. A detailed description of the software, its calibration, and accuracy is provided in Hsu (2000) and Grega *et al.* (2002). Because a variety of DPIV measurements were made for different flow conditions, details of specific parameters, such as time between laser pulses and vector spacing, are provided with the corresponding presentation of results.

3. Frequency and amplitude response characteristics of the inverted pendula

Frequency and amplitude response characteristics of the lower-mass-ratio cylinder are shown in figures 3 and 4, respectively. The difference in mass ratio is sufficiently small that the response characteristics of the higher-mass-ratio cylinder were virtually identical to those shown in figures 3 and 4. Measurements were made at the cylinder

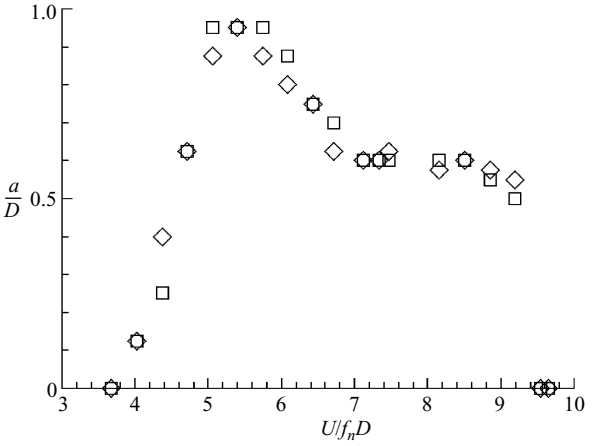

FIGURE 4. Maximum amplitude response characteristics of the acrylic cylinder undergoing vortex-induced-vibrations. See caption of figure 2 for definition of plot symbols.

mid-height, ~70 cm above the floor of the water tunnel. The square symbols denote data taken while incrementing upward through the velocity range. Diamonds denote measurements made while decrementing downward through the speed range. This provided insight into any hysteresis that may be present in the system.

It is readily observed from figures 3 and 4 that the cylinder response characteristics were virtually identical to those for elastically mounted cylinders. Following conventions chosen by Khalak & Williamson (1999), two distinct branches are observed. The initial excitation or upper branch, $3.8 < U^* < 7.0$, is characterized by vortex-shedding frequencies different from $S = 0.21$; in this case, $S \approx 0.18$. In addition, the interaction is characterized by strong energetic vortices shed very close to the cylinder and by a beating behaviour of the cylinder oscillations. This has also been referred to as *resonant synchronization*. The maximum amplitude in the resonant synchronization regime occurred at $U^* \approx 5.4$.

The lower branch, occurring for $7.0 \leqslant U^* \leqslant 9.2$, is characterized by oscillation amplitudes and frequencies which do not vary with U^*. In this lock-in regime, cylinder oscillation frequency and amplitude remained constant at $f^* \approx 1.2$ over a wide range of flow speeds. Flow visualization studies presented in Atsavapranee *et al.* (1999) and Voorhees (2002) indicated that in the classic lock-in regime, vortex shedding appeared rather disorganized in comparison to the resonant synchronization regime. This may be interpreted as the cylinder modulating the flow so that just enough energy was transferred from fluid to structure to maintain a fixed amplitude oscillation at the natural frequency. At the end of this regime, $U^* > 9.2$, the cylinder no longer vibrates in response to vortex shedding (until, of course, the second harmonic of the cylinder natural frequency is approached).

Figures 3 and 4 are also consistent with two recent investigations, Fujarra *et al.* (2001) and Kittagawa *et al.* (1999), in which cylinders were pinned at one end and free at the other. Fujarra *et al.* (2001) used a flexible cantilever in water for $1000 \leqslant Re \leqslant 2500$. The stiffness orientation in the cantilever primarily allowed transverse oscillations over the entire synchronization regime. (Streamwise oscillations were noted at flow speeds beyond synchronization.) Their cylinder had a low mass ratio, $m^* = 1.3$, and relatively high mass–damping, $m^*\zeta = 0.185$. The amplitude and frequency response had two branches and the average f^* during lock-in was 1.3.

4. Results and discussion: quasi-periodic beating phenomenon

As noted previously, data for this investigation were originally obtained as part of a reduced-order analytical modelling effort. This entailed phase-averaging time-resolved DPIV records containing the cylinder beating phenomenon. In order to do this, the $Re = 2300$ case in the resonant synchronization regime or upper branch was chosen for detailed measurement and analysis. This corresponds to the diamond-shaped data point at $U/f_n D \approx 4.4$ and $a/D \approx 0.4$ in figure 4.

This particular case was selected because of the relatively large oscillation amplitudes combined with the relative regularity of the beating. At lower reduced velocities or Reynolds numbers, the beating phenomenon becomes quite regular, but the oscillation amplitudes can be quite small. Between beat cycles, the amplitudes can be negligibly small. At higher reduced velocities, well-defined, quasi-periodic beat envelopes were relatively rare. One finds solitary beat patterns embedded in an otherwise irregular oscillation signal. An example of this type of irregular behaviour is visible in the first half of the second trace in figure 1; clearly there is nothing repeatable to focus on as 'characteristic' in that signal. The $Re = 2300$ case presents a good compromise where the oscillation amplitudes are large and repeated beat cycles occur fairly often. An hypothesis for why the beating phenomenon becomes more irregular with increasing reduced velocity is presented in the following section.

An ensemble of fifty individual DPIV velocity field sequences was assembled to examine the quasi-periodic beating phenomenon. Each sequence consisted of 225 consecutive velocity fields taken at 1/10 s intervals, or $\sim 1/13$ of a cylinder oscillation period, in a horizontal plane perpendicular to the axis of symmetry of the cylinder at rest. The location of the measurement plane was $\sim$70 cm above the floor of the test section, coinciding with the amplitude measurements. The spacing between vectors was 0.19 cm corresponding to $\lambda/D = 0.074$. The total duration of each sample was 22.5 s, or $\sim$17.3 cylinder oscillation periods.

One can clearly see from the cylinder position time traces in figure 1 that some criterion needed to be applied when capturing data sets. This was done by monitoring the output of the cylinder position sensor with a digital oscilloscope. After careful study of the cylinder oscillations, it became possible to anticipate when a beat-like event was about to occur. At those times, DPIV video images as well as the cylinder position sensor signal would be captured and stored to computer. The position sensor signal would also be monitored on the oscilloscope to see if the cylinder indeed underwent a beat cycle. The criterion for keeping the data set were that there had to be a symmetric beat envelope consisting of at least ten individual cylinder oscillations. In addition, the largest oscillation at the centre of the beat envelope had to be $\sim$20% larger than the oscillations at the beginning and end of the envelope. To remove the effects of small-scale fluctuations, e.g. shedding of Bloor vortices (for details, see Bloor 1964 or Wei & Smith 1986), phase averaging was done by centring on the peak of a beat cycle. For further details, please see Dong (2002).

4.1. *On the mismatch between vortex shedding and cylinder oscillation frequencies*

The first indication of differences between vortex shedding and cylinder oscillation frequencies was found during examination of phase-averaged time traces of individual terms in the mechanical energy transport equation, Dong *et al.* (2004). Two terms in the energy equation were particularly relevant to this discussion. These are the time rate of change of mechanical energy of the cylinder, $\partial(KE + PE)_{cylinder}/\partial t$, and the flux of fluid kinetic energy across the boundaries of a fixed control volume surrounding the cylinder (including some fluid as well). The mathematical expression for this latter

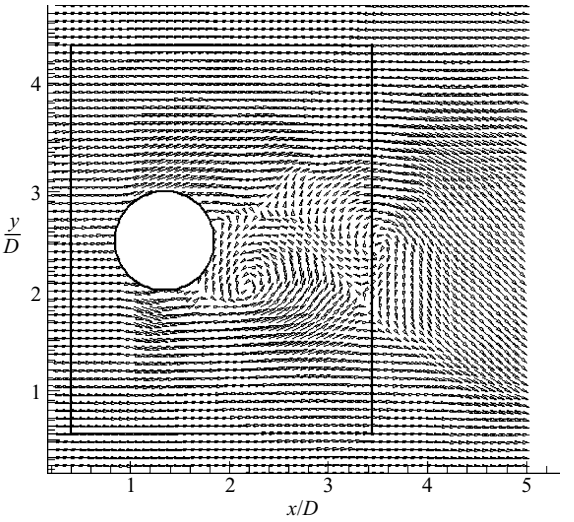

FIGURE 5. Instantaneous DPIV vector field showing flow around the acrylic cylinder. Flow is left to right. The control volume used for computing fluid kinetic energy flux calculations is shown as a black rectangle.

term is $\int \frac{1}{2}\rho \boldsymbol{V}^2(\boldsymbol{V}\cdot \mathrm{d}\boldsymbol{A})$, and is denoted here as $(KE)_{fluid}$ *flux*. A sample instantaneous vector field with the control volume used in this analysis is shown in figure 5.

The significance of these terms is that the time derivative of the cylinder kinetic energy will, obviously, be correlated to the cylinder motion. In fact, a time trace of $\partial(KE + PE)_{cylinder}\partial t$ should be exactly 180° out of phase with the cylinder position signal. The fluid kinetic energy flux term turned out to be a good metric for tracking the vortex shedding frequency. Oscillations in the time-dependent $(KE)_{fluid}$ *flux* term were correlated with the passage of a Kármán vortex across the downstream face of the control volume. For details of this, see Dong *et al.* (2004).

Spectra computed from phase-averaged time traces of these two energy transport terms are presented in figure 6. As noted earlier, data acquisition was conditionally sampled to capture complete beat cycles during quasi-periodic beating. The key feature of figure 6 is that the spectral peaks of the cylinder energy derivative and the fluid kinetic energy flux terms do not coincide; there is a slight mismatch between the two peaks of approximately 0.1 Hz. It is important to reiterate that this frequency difference can be detected only within the beat period. If one takes long time averages of vortex shedding and cylinder oscillation frequencies, as has typically been done, the frequencies are and have been found to be identical. The physical implications of this will be addressed in §4.2 and §4.3.

To independently validate the observed frequency difference, space–time correlation plots, shown in figures 7 and 8, were developed. Figures 7 and 8 each contain the overlay of two plots. The first is the phase-averaged cylinder position *vs.* time trace, shown as a solid white sinusoidally varying signal. Observe the characteristic beating envelope with a maximum at the centre of the trace. The same phase-averaged position *vs.* time trace appears in both figures. Superimposed on the cylinder position trace are space–time plots showing the passage of phase-averaged axial vorticity, Kármán vortices, past a fixed streamwise station as a function of time. The abscissa in the plot is time, t, while the ordinate is spanwise position, y. To generate these plots, the distribution of axial vorticity, ω_z, across the cylinder wake at a fixed location,

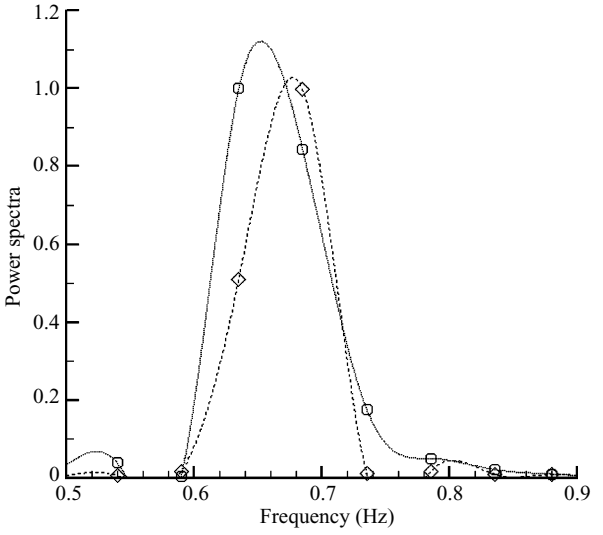

FIGURE 6. Power spectra of time rate of change of cylinder energy, $\partial(KE + PE)_{cylinder}\partial t$ (diamonds), and fluid kinetic energy flux, $(KE)_{fluid}$ *flux* (squares). Only the portions of the spectra with non-zero frequency components are shown.

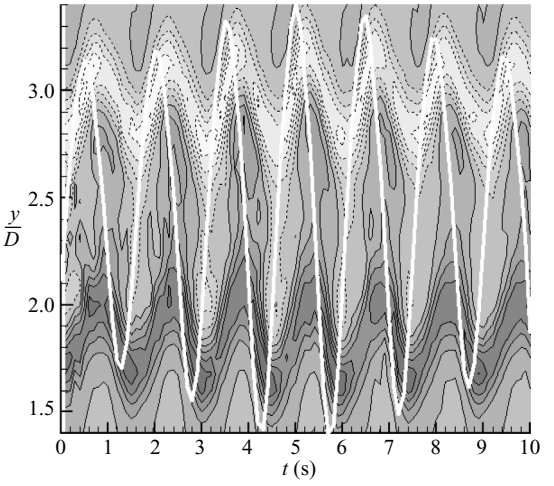

FIGURE 7. Space–time contour plots showing the correlation between vortex shedding and cylinder oscillations: cross-stream position *vs.* dimensional time. Plots were obtained using spanwise distributions of vertical vorticity at $x/D = 2.3$ (see figure 5) at successive times through a phase-averaged beat cycle. The cylinder position *vs.* time trace is superimposed as a solid white line.

$x/D \approx 2.3$ for figure 7 and $x/D \approx 3.0$ for figure 8, was extracted from each phase-averaged vector field in the beat cycle. This yielded time-dependent functions, $\omega_z(y, t)$, plotted as shaded contours.

The purpose of figures 7 and 8 is to study the relation between Kármán vortex shedding and cylinder oscillations. It is possible to compare relative spacing between peaks in the cylinder position *vs.* time trace and the corresponding centre of vorticity. In principle, if a Kármán vortex were shed before the cylinder reaches its point of local maximum deflection, the vorticity contours will be located to the left, i.e.

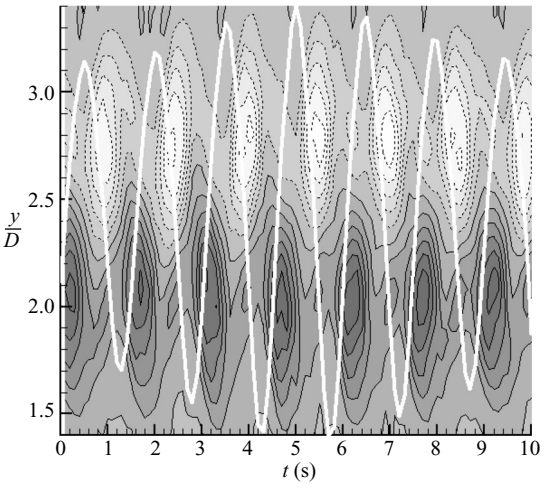

FIGURE 8. As figure 7 but at $x/D = 3.0$.

at an earlier time, than the local maximum in the cylinder position *vs.* time trace. Similarly, if the Kármán vortices shed at the same time or after the cylinder reaches its peak deflection, vorticity contours and position *vs.* time trace would coincide or the vorticity would lag the peak in cylinder position, respectively.

In reality, this is too simplistic because there is a delay as the forming Kármán vortex advects downstream away from the cylinder. Without a specific criterion for when a vortex 'sheds' from the cylinder, the exact phase relationship between shedding and oscillation cannot be quantified. One can, however, get a sense of where vortices detach from the cylinder near wake by comparing iso-vorticity contours in figures 7 and 8. In figure 7, one can see that the vorticity contours associated with the Kármán vortices form sinusoidal waveforms across the entire plot. Closer examination reveals small closed contours close to the extrema of the cylinder position *vs.* time trace. While this may be interpreted as the time at which vortices are shed from the cylinder, this would have a high degree of subjectivity associated with it.

Figure 8, on the other hand, clearly shows closed vorticity contours. This indicates that coherent Kármán vortices have become detached from the cylinder. To precisely determine from figure 8 the time at which the vortices begin to move downstream from the cylinder, one would need to know the vortex advection speed.

To verify the difference between vortex shedding and cylinder oscillation frequencies, one can use the data in figure 8 to measure the time delay between a peak in the cylinder position trace and the centre of the corresponding vortex. This was done for each of the first six cylinder oscillations appearing in figure 8. In particular, the focus is on the clockwise, negative-sign vortices appearing in the upper half of the figure. For each oscillation, the extreme point of cylinder deflection and the approximate center of the Kármán vortex shed during that oscillation cycle were located. For the latter, the approximate centre of the largest and nearest vorticity contour was identified. Using magnification tools in the plotting program, the time between these two events was measured. It was found that the time delay between maximum cylinder deflection and passage of the vortex centre increased from 0.41 s for the first oscillation to 0.48 s for the sixth oscillation. Measurements made on other oscillation peaks demonstrate that the trend is consistent across the entire phase-averaged beat cycle. Thus, once again,

it is seen that the vortex shedding frequency is lower than the cylinder oscillation frequency during a beat cycle.

4.2. *Effects of modulated cylinder amplitude on Kármán vortex strength*

As a result of the preceding analyses, one can conclude that the quasi-periodic beating phenomenon arises, at least in part, from differences between vortex shedding and cylinder oscillation frequencies. It is noteworthy that the frequency difference is of the order on 0.1 Hz and the beat period is of the order of 10 s. While the temporal resolution of the measurements limits the precision of this observation, it is consistent with both the spectra in figure 6 and the beat period observed in the long-time cylinder position *vs.* time traces shown in figure 1.

The existence of beating raises the question of whether a modulation of Kármán vortex strength accompanies the cylinder amplitude modulations. To address this, temporal variations in vortex strength were calculated from the DPIV data. This was done by defining a rectangular control volume which moved with the oscillating cylinder. A variety of different sized and positioned control volumes were tried. The one that seemed to produce the cleanest and most consistent results was a contour which was centred on the cylinder in the cross-stream direction, with its upstream and downstream faces passing through the cylinder and $1\frac{1}{4}$ diameters downstream of the cylinder, respectively. Using flow visualization studies, described in Atsavapranee *et al.* (1999), it was determined that the Kármán vortices behind the oscillating cylinder formed immediately downstream of the cylinder. This was due to the fact that, because of the oscillatory motion, the flow relative to the cylinder was at an angle to free-stream direction. Thus, placing the control volume symmetrically behind the cylinder captured the Kármán vortex formation.

Estimates of vortex strength then could be obtained in a straightforward manner by computing the circulation around the rectangular contour described above at each time step in the DPIV sequence. For the upstream face of the control volume, the local velocity was prescribed to be the instantaneous speed of the cylinder. This is, of course, a very approximate calculation. There is not a built-in assessment of what is actually contained inside the control volume at any instant of time. However, it is an objective calculation providing, therefore, at least a qualitative sense of vortex strength as a function of time through the phase-averaged beat cycle.

Comparisons between cylinder oscillations and temporal variations in phase-averaged vortex strength, i.e. circulation, are shown in figure 9. The phase-averaged cylinder oscillation signal appears as a dotted line while the circulation signal is a solid black line. It is interesting to note that while the cylinder position beat envelope is symmetric about $t = 5.0$ s, the circulation signal does not exhibit the same symmetry. Rather, vortex strength appears greatest one or two oscillation cycles before the largest cylinder deflection. On average, then, the Kármán vortices are stronger when the peak cylinder oscillation amplitude is increasing than when the beating cycle envelope is decreasing. Further, it appears that the largest cylinder deflection occurs one to two cycles after the strongest Kármán vortex has been shed. Thus, beating behaviour in the synchronization regime for low-mass-ratio cylinders is due not only to a mismatch between the vortex shedding and oscillation frequencies, but also to a modulation in Kármán vortex strength.

4.3. *Thoughts on the irregularity of cylinder amplitude in the synchronization regime*

The data presented in this paper, particularly the frequency results, raise an interesting question about the irregularity of the cylinder deflection traces shown in figure 1.

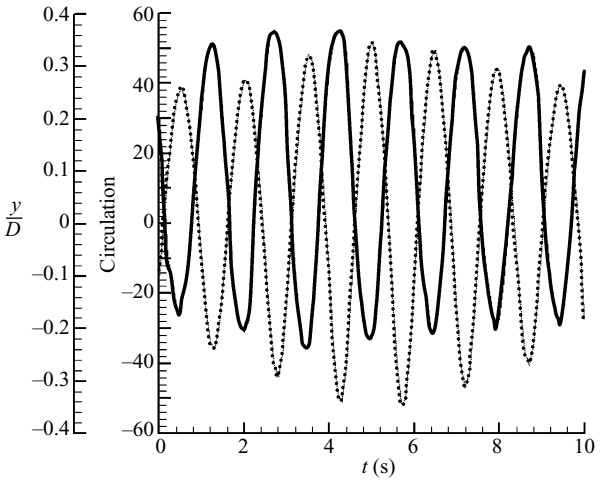

FIGURE 9. Comparison of vortex strength, i.e. circulation (solid black line), in the cylinder near wake with cylinder oscillation amplitude (dotted line) as a function of time in the phase-averaged beat cycle. Note that vortex strength is modulated, with the maximum strength occurring 1–2 oscillations before the largest amplitude deflection.

Specifically, why does beating appear to abruptly end after a small number of beat cycles? The remainder of this section includes thoughts and a hypothesis on the observed irregularities.

It is well known that two harmonic oscillators with different fundamental frequencies will combine to form a beating signal where the beat frequency is equal to the difference of the two fundamental frequencies. That this is the case for the vortex shedding and cylinder oscillation frequencies is readily apparent from the phase-averaged oscillation trace, shown in figures 7–9, and the spectra of fluid kinetic energy flux and cylinder oscillation shown in figure 6. It was noted earlier that the difference frequency appears to be on the order of 0.1 Hz. This matches the $\sim$10 s beat period observed in figure 1.

Unlike the mathematical system of two mismatched oscillators, however, there are physical constraints on the VIV problem. That is, whereas two sine waves with differing frequencies will go in and out of phase over long periods of time, it is physically unrealistic for vortices, which are typically shed when the cylinder has deflected to one side, to shed when the cylinder has deflected to the other side. This is shown schematically in figure 10, which is a sketch of a cylinder oscillation *vs.* time trace. Associated with each positive peak in the trace, there is a little schematic of a cylinder shedding a clockwise Kármán vortex. Each cylinder schematic has been placed on the trace at the time the vortex is shed. Cross-hairs have been drawn on the cylinders and located on the trace to facilitate this image. Note that this is a hypothetical picture because exact information about the precise relation between oscillation and vortex shedding times is not known.

Figure 10, then, was constructed to illustrate the physical relation between vortex shedding and cylinder oscillation. If both the shedding and oscillation frequencies were the same, every vortex would be shed at the same relative time in each oscillation cycle. However, since the vortex shedding rate is slower than the oscillation frequency for the conditions of this experiment, one should expect that each successive vortex

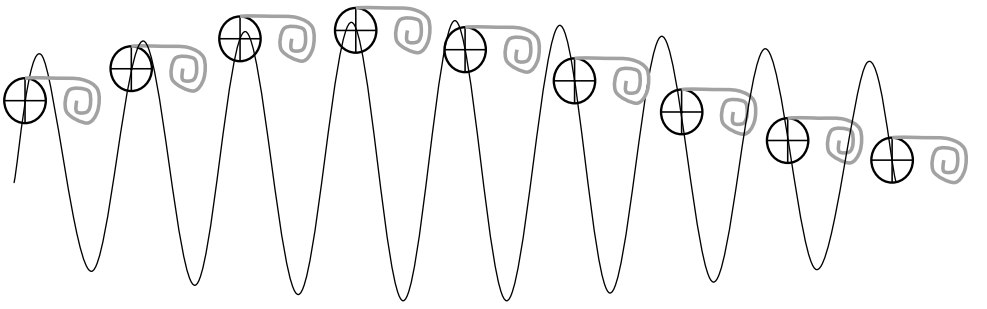

FIGURE 10. Cartoon showing the effects of differences between vortex shedding and cylinder oscillation frequencies. The sinusoidal line represents a modulated cylinder oscillation trace. Circles with cross-hairs and grey curved lines show how there will be an increasing delay in Kármán vortex shedding relative to the local maximum in the cylinder motion if the shedding frequency is lower than the oscillation frequency. Note that this cannot be sustained for more than a few beat periods, depending on the magnitude of the difference frequency.

would be shed later and later in the oscillation cycle. The steadily increasing delay in vortex shedding is illustrated in figure 10.

The logical extension of this increasing delay would be that clockwise, negative-sign vortices would eventually be shed when the cylinder deflects in the opposite direction. However, such a flow would be decidedly non-physical. It would necessitate roll-up of vorticity on the wrong side of the cylinder. An alternative way of looking at this is that the low-pressure Kármán vortex would push against the cylinder. Thus, before this was to happen, the flow must 'reset' such that vortices are shed on the 'correct' side.

While detailed studies of the 'correction' process have not been made, it is hypothesized that it occurs quite rapidly, within one or two cylinder oscillations. There is no evidence of a corresponding quasi-periodic beating cycle during which the vortex shedding frequency is higher than the cylinder vibration rate. Rather, the long-time oscillation signal in figure 1 shows abrupt departures from beating after a few beat periods. Examination of LIF flow visualization sequences also revealed moments when an irregular looking vortex would be shed from the cylinder. Such events, when considered on their own, would appear random and singular in nature. However, in the light of the frequency mismatch described in § 4.1 and the implications illustrated in figure 10, they can be interpreted as being part of this 'correction'.

This, of course, does not mean that the cylinder would immediately return to beating. Indeed, figure 1 reveals extended periods of time when the cylinder is not exhibiting either classic beating behaviour or constant-amplitude oscillations. The dynamics of how the cylinder transitions into quasi-periodic beating is an open and probably quite complex issue.

5. Results and discussion: three-dimensionality in the cylinder wake

The second focus of this paper is three-dimensionality in the cylinder wake. Specifically, the effects of the inverted pendulum motion on Kármán vortex shedding and the interaction of the Kármán vortices with the free-surface are of particular interest. As a first approach to studying this problem, two-colour LIF and food colour flow visualization studies were conducted 6.7 cm, 37.2 cm and 67.6 cm below the free-surface. This corresponds to $z/D = -2.6$, –14.6 and –26.6, respectively. For

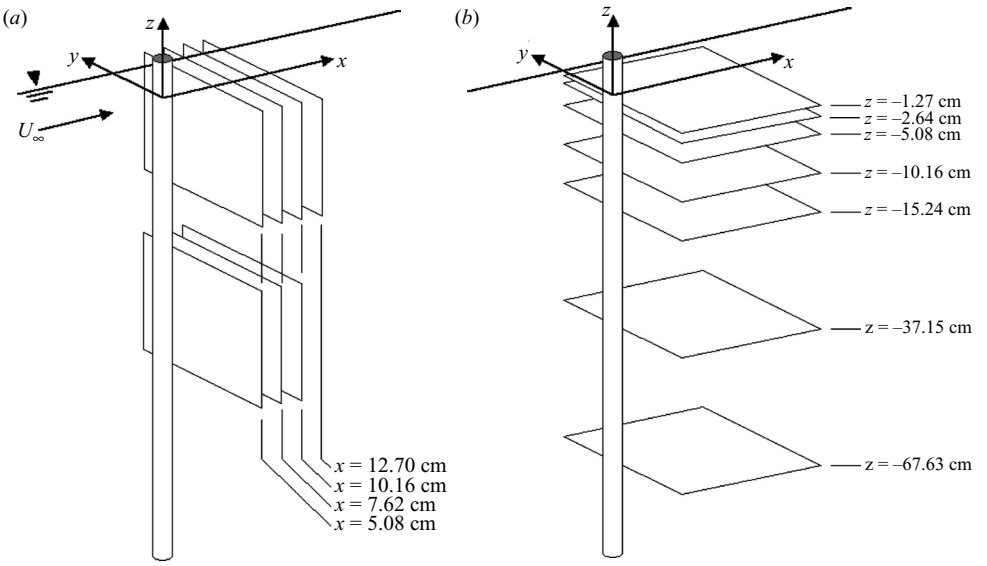

FIGURE 11. Schematic drawing showing the fourteen different DPIV measurement planes, both orientation and location, used to quantify three-dimensionality in the cylinder wake.

the LIF studies, the fields of view were of the cylinder near wake, including the downstream half of the cylinder, spanning ~ 6 cylinder diameters in the stream direction and ~ 5 diameters in the transverse direction. Five minute video sequences were recorded for each combination of flow speed and visualization location. The range of Reynolds numbers, based on cylinder diameter and free-stream velocity, extended from 2300 to 6800. Depending on flow speed, five minutes corresponded to 280–380 vortex-shedding periods. Visualizations were conducted both increasing and decreasing through the Reynolds number range to note any hysteresis effects. LIF records were used to extract Kármán vortex-shedding frequency and cylinder oscillation amplitude frequency.

Side-view food-colour visualizations provided insight into wake three-dimensionality. Fields of view for these studies were approximately 14 and 12 diameters in the x- and z-directions, respectively. Ten minute video sequences of VIV were recorded for five different Reynolds numbers from 3000 to 3800. One additional case was recorded at $Re = 3800$ in which the cylinder was fixed at its neutral position. Recordings were examined for the presence and nature of vertical flows.

In addition, fourteen sets of DPIV measurements were made in both horizontal and cross-stream planes in the cylinder near wake. A single speed was examined where the non-dimensional reduced velocity, $U^* = U_\infty f_n / D$, was 4.9, or $Re = 3400$. This was in the synchronization regime of the cylinder response characteristics, also referred to as the 'upper branch' in Khalak & Williamson (1999). A schematic drawing showing the different measurement planes and their locations is shown in figure 11. Each rectangle in the figure represents a measurement field typically $\sim 5 \times 5$ cylinder diameters in size. End-view measurements, horizontally centred about the mean cylinder rest position, were made at up to four downstream positions and two distances below the free-surface. Horizontal plan-view measurements were made at seven locations below the free-surface.

Nominally, fifteen individual DPIV data sets were recorded at each of the fourteen measurement locations. Each set was 15 s in duration comprising 225 DPIV image pairs and 4500 cylinder displacement samples. Data were conditionally captured when the cylinder underwent quasi-periodic beating as described in § 4. In reference to this cycle, 'peak' denotes the maximum amplitude and 'trough' or 'neck' refer to the minimum amplitude. The final ensemble of DPIV sequences was selected based on the criterion that they each contain one complete beat cycle. For these measurements, the spacing between adjacent vectors was ~ 0.1 cm or $\lambda/D = 0.04$.

Each individual 15 s DPIV data sequence was reduced in length to include one beating cycle centred on the trough. This was done by locating the trough using the position sensor signal (sampled at 300 Hz) and identifying the DPIV vector field closest in time to the trough. Note that the temporal uncertainty associated with considering that DPIV vector field to be located at the trough is ± 0.033 s. An 11 s DPIV sequence was then selected by including 5.5 s of data on either side of the trough. Once each sequence had been conditionally sampled, phase averaging was achieved by simply ensemble averaging conditionally sampled sequences. Because of the tremendous amount of data (165 vector fields per sequence $\times 14$ measurement locations/orientations $\times$ 10 sequences per ensemble), only ten sequences were included in each phase average; see Voorhees (2002) for details. The principal advantage of phase averaging in this study was the ability to reconstruct the three-dimensional topology of the phase-averaged Kármán vortices. This is described in the following paragraph.

Temporally resolved, three-dimensional, phase-averaged reconstruction of Kármán vortices was done using plan-view vorticity data, ω_z, from six spanwise locations $z/D = -1.0$, -2.0, -4.0, -6.0, -14.6 and -26.6. As with all other DPIV data, the reduced velocity, U^*, was 4.9. Vortex cores were located using an adaptive three-dimensional feature tracking algorithm developed by Wang (1999). By setting a vorticity threshold, regions of large vorticity could be located with the perimeter being denoted by the threshold value. The centroid of the vortex (or region of vorticity) was then determined using a weighting function over the entire structure based on the position and magnitude of vorticity. A rough estimate of the uncertainty associated with the vortex tracking was made using unaveraged velocity fields. Far from the free-surface the root-mean-square vortex location uncertainties in the streamwise and cross-stream directions (non-dimensionalized by cylinder diameter) were 0.12 and 0.02, respectively. Near the free-surface the r.m.s. vortex position uncertainties were 0.43 and 0.11 in the streamwise and cross-stream directions, respectively. The Kármán vortices were reconstructed by connecting vortex cores in the spanwise direction after first individually locating the centroids of all vortices of each measurement plane.

5.1. *Spanwise variations in the Kármán vortices*

In the present study, the cylinder's maximum deflection angle was less than 1.5°, and the response characteristics resemble those of elastically mounted cylinders. As discussed in Dong *et al.* (2006), it is permissible to model the VIV for this structure using a two-dimensional flow assumption. In reality, however, it is intuitively obvious that the local cylinder displacement increases linearly in the positive z-direction. It is therefore quite possible that spanwise variations (or three-dimensional flows) may be induced by the inverted pendulum-like motion. The focus of this section is on the answer to that question.

To explore spanwise flow variations, LIF studies were conducted in horizontal planes at various locations along the cylinder span. In addition to the LIF sequences

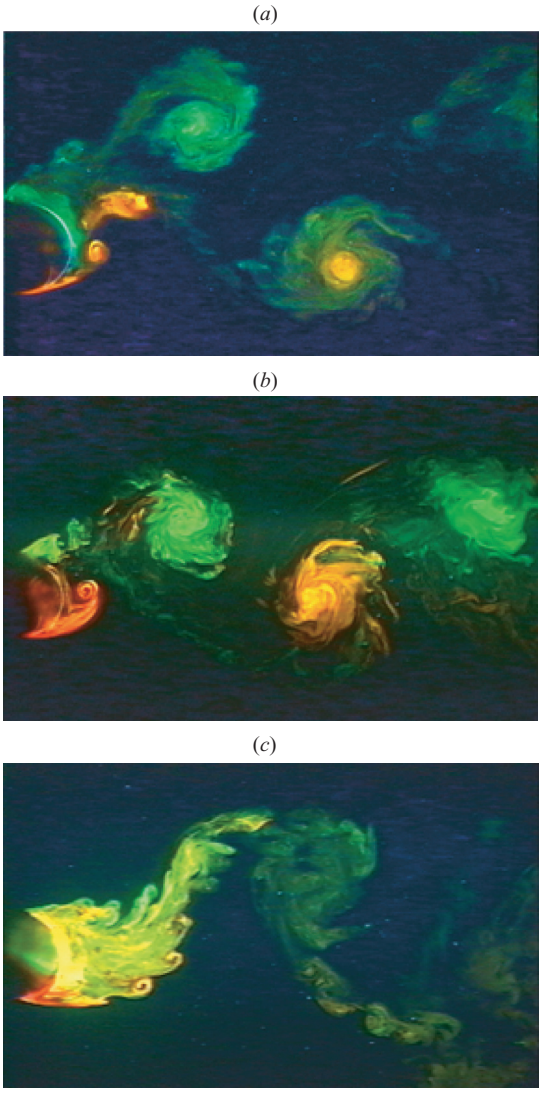

FIGURE 12. Three instantaneous LIF flow visualization images showing flow patterns behind the cylinder at the same relative location in a beat cycle. Flow is left to right with the reduced velocity set at 4.9. (*a*) $z/D = -2.6$; (*b*) $z/D = -14.6$; (*c*) $z/D = -26.6$.

acquired at the cylinder mid-height, $z/D = -14.6$, visualizations were also performed toward the top of cylinder, $z/D = -2.6$, close to the free-surface, and at the bottom $z/D = -26.6$, near the leaf spring. These studies were conducted at a single flow speed, $U^* = 4.9$. Figure 12 includes single still images from each location with figures 12(*a*), 12(*b*) and 12(*c*), corresponding to $z/D = -2.6$, –14.6 and –22.6, respectively. For publication cost reasons, these photographs have been reproduced in black and white. Flow is left-to-right with the cylinder located on the left edge of each image. Note that the images shown in figure 12 were taken at the same relative time in the cylinder oscillation cycle.

If there were no significant three-dimensionality along the length of the cylinder, the three photographs comprising figure 12 should look similar if not identical; recall

that each photograph was taken at the same relative time in the oscillation and beat periods. Comparison of the three images, however, reveals marked differences. Figures 12(*a*) and 12(*b*) show distinctly separated regions of dye in the wake indicating that dye has coalesced into Kármán vortex cores. In figure 12(*c*), however, dye entrainment between vortices is clearly visible. DPIV measurements, presented in Voorhees (2002), also confirm that vortex strength varies with depth; vorticity increases approaching the free-surface where the local oscillation amplitude is greatest.

In addition, one can observe differences in wake width, or transverse vortex spacing, between figures 12(*a*) and 12(*b*). In figure 12(*a*), where the Kármán vortices are closest to the free-surface and the cylinder oscillation amplitude is greatest, the spanwise separation (i.e. the vertical separation distance in the photographs) is correspondingly the largest. For comparison, note that the cross-stream separation between successive counter-rotating Kármán vortices in figure 12(*b*) is approximately half the separation distance in figure 12(*a*).

Finally, it interesting to note that near the free-surface, $z/D = -2.6$, dye was observed to both disappear and reappear from the image plane in a burst-like manner. This was not observed farther away from the free-surface at $z/D = -14.6$ and –26.6. This cannot, of course, be seen in single still images, such as those shown in figure 12. This observation came from examination of the video records directly.

The possibility that spanwise variations in vortex strength and spacing may be due to amplitude-dependent mechanisms, such as cellular shedding, was considered. The widely cited amplitude response plot first introduced in Williamson & Roshko (1988) suggests that two modes of vortex shedding should exist along the span. Along the lower part of the cylinder, one would observe the '2S' mode, while '2P' would occur closer to the free-surface. The demarcation point would be located where the local dimensionless oscillation amplitude, A^*, was 0.5. Note that for the present study, the local value of A^* where the cylinder crossed the free surface was 0.8. However, food colour injected from the dye slots at different cylinder heights did not reveal evidence of spanwise cells; it was possible to visually track dye as it was pumped up (and down) in the Kármán vortex cores. This is described in greater detail in the following section. In addition, both the DPIV data and the flow visualization studies indicate that only the '2S' mode exists along the entire span. The origins of the spanwise variations are therefore more complicated than simple variations in local oscillation amplitude. This is a significant point of difference between the inverted pendulum of the present study and two-dimensional elastically mounted cylinder experiments.

5.2. *Axial flows along the Kármán vortices*

The logical next step was to directly quantify/verify the existence of three-dimensional flows induced by the pendulum-like motion of the cylinder. At the outset, it would be instructive to conduct a thought experiment regarding the nature of axial flows one might expect to be associated with vortices shed from an inverted pendulum. Both visual and quantitative evidence indicated that the local vorticity magnitude, $\omega_z(z)$, increases along the axis of any given Kármán vortex, beginning at the pinned end and approaching the free-surface. This is a direct result of the increase in local oscillation amplitude in the positive z-direction. Because $\partial\omega_z/\partial z > 0$, one would expect a concomitant negative pressure gradient, $\partial p/\partial z < 0$, which would pump fluid upward toward the free end of the cylinder. This axial flow would necessarily have to be disrupted, however, by the free-surface. It is difficult to predict the effect of the free-surface on the axial flows.

Very strong upward flows associated with the Kármán vortices were indeed observed when food colour was injected at the cylinder mid-height and close to the pivot point, $z/D = -14.6$ and –26.6, respectively. The strength of the upflows varied through the cylinder beating cycle. The most energetic upflows transported dye several cylinder diameters above the dye injection plane within only a few vortex rotation periods. However, no downflows were observed at these visualization locations.

In contrast, dye injected from the upper location at $z/D = -2.6$ was observed to be ejected both toward and away from the free-surface. In addition, periods of upflows and downflows appeared to alternate in a quasi-periodic behaviour that was correlated with the beat cycle. By superposing an oscilloscope trace showing instantaneous cylinder position onto the flow visualization video signal, direct correlation of up- and downflows with the beat cycle could be achieved.

Correlation was done by first classifying the beat cycle into four regions: peak, trough, increasing amplitude, and decreasing amplitude. The next step was to define an indicator function, Φ, such that $\Phi = -1$ and $+1$ for downflow and upflow respectively. If no significant vertical flow was observed Φ was set to zero. Ensemble averages of Φ were generated for each of the four regions using an ensemble of 40 beat cycles. Each ensemble average, $\langle \Phi \rangle$, represents the probability that an up- (or down-) flow would occur in each of the four regions of the beat cycle.

The results of this analysis are presented in figure 13. There are two parts to this figur: (*a*) shows cylinder displacement versus time for one beating cycle; (*b*) shows the type of axial flows observed at each beating cycle location. The four regions in the upper plot have been numbered (i) to (iv) corresponding to peak, decreasing amplitude, trough, and increasing amplitude. The ordinate of the lower plot is $\langle \Phi \rangle$ for each region (i) to (iv). Error bars represent the r.m.s. of $\langle \Phi \rangle$. Figure 13 clearly indicates that upflows are associated with increasing amplitude while downflows are associated with decreasing amplitude. In addition, on average, no axial flows occur in the peak or trough regions of the beat cycle.

To further quantify these axial flows, end-view (y, z-plane) DPIV measurements we re conducted at the locations shown in figure 11. Figure 14 shows a sequence of six instantaneous velocity vector fields measured at the mid-height plane, which is centred at $(x/D,\ y/D,\ z/D) = (2.0,\ 0,\ -14.6)$. The time between successive frames is 0.067 s. The sequence in figure 14 shows the passage of a counter-clockwise rotating vortex, i.e. positive sign vorticity, through the measurement plane. Notice that the vector plots are shifted slightly left of centre to focus on this vortex; $y/D = 0$ is the wake centreline.

By way of orientation, consider a positive-sign, vertical vortex ($+\omega_z$) carried in the x-direction through a vertical measurement (y, z)-plane. As the vortex approaches the measurement plane, the circumferential velocities would appear as a vertical band of horizontal velocities oriented in the positive y-direction. When the vortex is centred on the measurement plane, the circumferential velocities will be normal to the measurement plane. Flow will be into and out of the page to the right and left of the vortex axis, respectively. After the vortex centre has moved downstream of the measurement plane, the circumferential flow will change direction and go from right to left.

This global motion is clearly evident in figure 14. As the vortex begins to move through the measurement plane, $x/D = 2.0$, one can see a vertical band of velocity vectors, between $y/D \approx -1.5$ and $y/D \approx +0.5$, pointing principally in the positive y-direction. This can be seen in figure 14(*a–c*), most strongly in figure 14(*c*). And

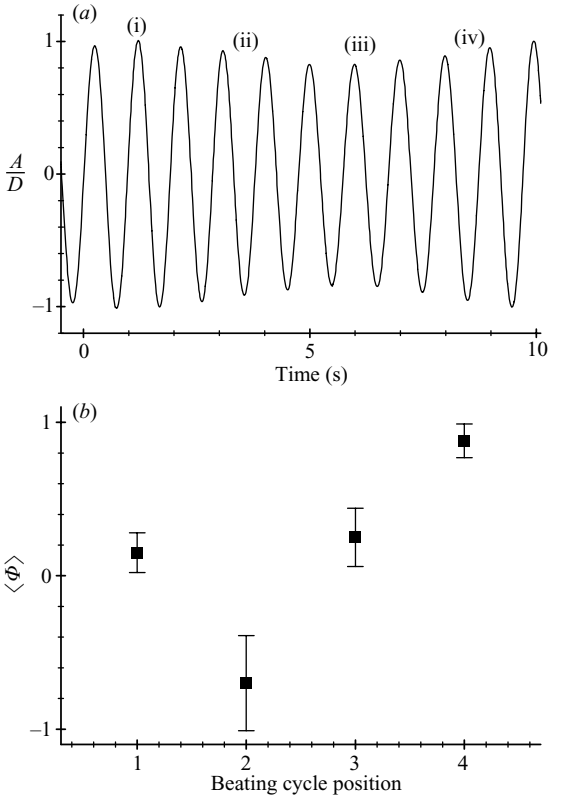

FIGURE 13. Mean indicator values for vortex axial flow direction, $\langle \Phi \rangle$, as a function of temporal location in the cylinder beating cycle. Positive and negative values of $\langle \Phi \rangle$ signify upward and downward flows, to and from the free surface, respectively. Data were taken using side-view food-colour flow visualization video sequences where dye was injected at $z/D = -2.6$. (*a*) Cylinder displacement versus time for one beating cycle. (*b*) Type of axial flow observed.

after the core passes through the plane, figures 14(*e*, *f*), the direction of the cross-flow reverses, pointing in the negative y-direction.

It appears that in figure 14(*d*) the Kármán vortex core is roughly centred front-to-back on the measurement plane. This is evidenced by the lack of cross-stream flow in either direction. The salient feature of this particular vector field, then, is the strong organized upward motion toward the free-surface. It is believed that these motions are, in part, responsible for the energetic up-welling and down-welling motions observed in the food colour visualization studies.

Embedded in each of the vector fields comprising figure 14 are smaller-scale turbulent motions. Notice for example the counter-rotating vortex pair in figure 14($a - c$) centred at $(y/D, z/D) \approx (0, -13.6)$. This is an example of 'Bloor' vortices discussed in Wei & Smith (1986); they are clearly visible in the LIF photographs in figure 14(*c*). Wei & Smith (1986) determined that Bloor vortices develop spanwise waviness and are stretched and reoriented into the stream direction.

5.3. *Space–time evolution of three-dimensional Kármán vortices*

A compact and insightful way to examine the aggregate of DPIV sequences is to plot the data using space–time coordinates. This was done by tracking the

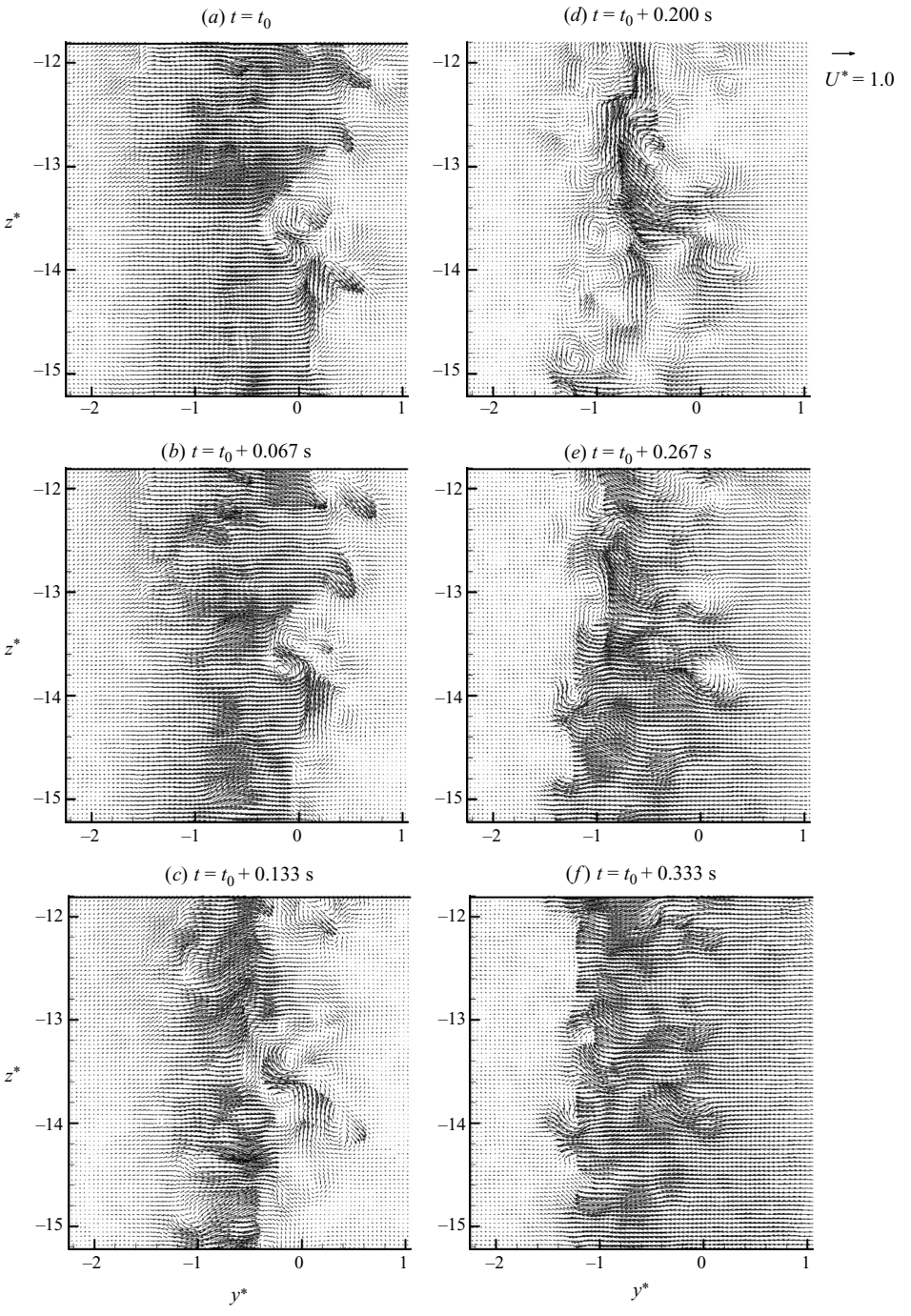

FIGURE 14. Sequence of six consecutive DPIV vector fields in a cross-stream plane located at $x/D = 2$ and $z/D = -14.6$. The mean flow is out of the page. $y/D = 0$ denotes the cylinder rest position in the cross-stream direction. Time between successive vector fields in 1/15 s. The sequence shows the passage of a Kármán vortex through the measurement plane. Note the change in cross-stream flow direction as the vortex approaches and then passes. Also note the upflow in the vortex core

.

temporal evolution of fluid quantities along a line defined by the intersection of phase-averged horizontal, x, y, and end-view, y, z, DPIV sequences. Simultaneously plotting transverse, y, distributions of both axial vorticity, ω_z, and axial or free–surface normal velocity, u_z, at each time in the phase-averaged sequence resulted contour plots like those shown in figure 15. For the complete set of space–time plots, see Voorhees (2002).

Lines in figure 15 show contours of constant axial vorticity. Solid lines indicate positive vorticity while dotted lines denote negative values. Non-dimensional vorticity magnitudes, $\omega_z D/U_\infty$, are provided on the contour labels. The contours show the direction and magnitude of axial flows at each transverse location and time. Vertical velocity magnitudes have been non-dimensionalized by free-stream speed. White and dark grey contour levels indicate upflows and downflows, respectively. Observe that the maximum magnitudes exceed 25% of the free stream. It is also important to note that time has been reversed in figure 15 to give the effect of flow moving from left to right. The oldest eddies, shed at $t^* = 0$, appear on the right of the plot, while eddies shed most recently, $t^* \approx 12$, appear on the left. Also recall that $y/D = 0$ is defined to be the wake centreline or the rest position of the cylinder axis.

Figure 15 shows the space–time evolution of axial vorticity and axial flow along horizontal lines at $x/D = 3.0$ for four different depths below the free surface, $z/D = -1.0$, -2.0, -4.0 and -14.6. The three important features to compare between plots at different depths are transverse vortex spacing, modulation of wake width, and direction and magnitude of axial flows. In the first instance, examination of iso-vorticity contours with increasing distance from the free-surface reveals that wake width decreases significantly with depth. This is most pronounced within six diameters of the free-surface as will be discussed later. Closest to the free-surface, $z/D = -1.0$, opposite-sign vortices are 3–4 cylinder diameters apart. At the cylinder mid-height, however, figure 16(d), the maximum transverse vortex separation is only one diameter.

The second important feature in figure 15 is the modulation in wake width as a function of distance from the free-surface. The strongest modulation appears to be located at $z/D = -4.0$, seen in figure 15(c). Note that this is also the location where the strongest downward axial flows were observed. Closest to the free surface, however, the wake width appears to be relatively constant.

Finally, consider the magnitude and direction of axial flows along the cylinder span. Figure 15(a) shows the phase-averaged evolution of vertical flows closest to the free surface. Note that vertical flows are predominantly toward the free surface with the strongest upflows being closely associated with the Kármán vortex cores. However, it is interesting to note that significant axial flows are also observed across the wake. These are reminiscent of free-surface 'scars' between counter-rotating surface-parallel vortices described by Sarpkaya & Henderson (1985) and Hirsa & Willmarth (1994). However, the features in the present experiments are principally directed upward toward the free surface, while 'scars' arise from sub-surface transverse vortices which transport fluid both to and from the surface.

Only one diameter farther below the surface, at $z/D = -2.0$, there is an equal probability of detecting upflows or downflows. It can also be seen that upflows and downflows appear in tandem, with an upflow occurring before, i.e. downstream, of a downflow. This is physically consistent with the observation that Kármán vortices lean outward away from the wake centre near the free-surface. Given the sign of rotation of the vortices, the outward lean would give rise to upflow on the downstream, leading side of the vortex and downflows would be observed on the upstream, trailing side.

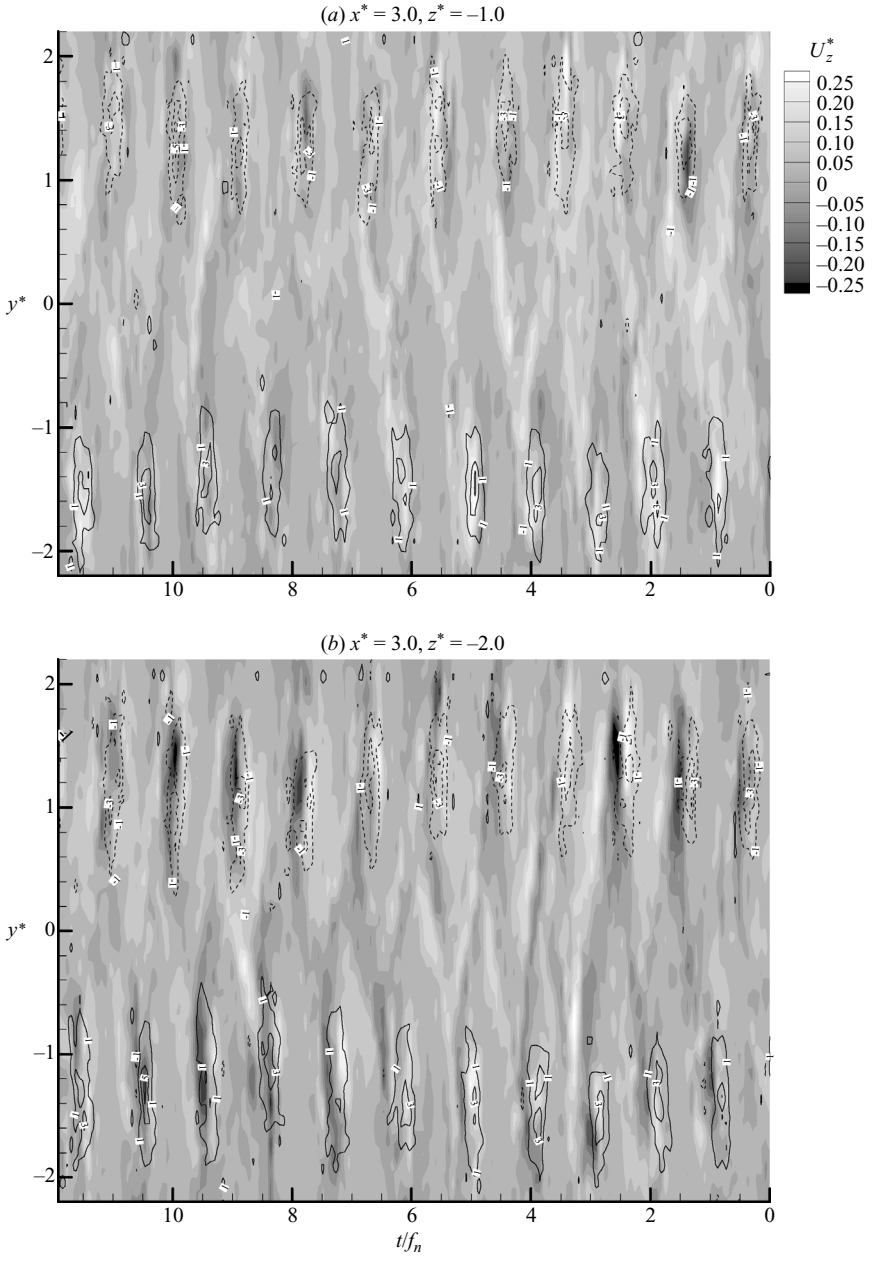

FIGURE 15(*a*, *b*). For caption see facing page.

At the cylinder mid-height, figure 16(*d*), vertical motions are primarily directed up toward the free-surface. This is consistent with the thought experiment presented earlier anticipating that axial flows would be induced by pressure gradients toward the free end of the pendulum. It is also in agreement with the food-colour visualization studies indicating that only upward flows were observed at the cylinder bottom and mid-height.

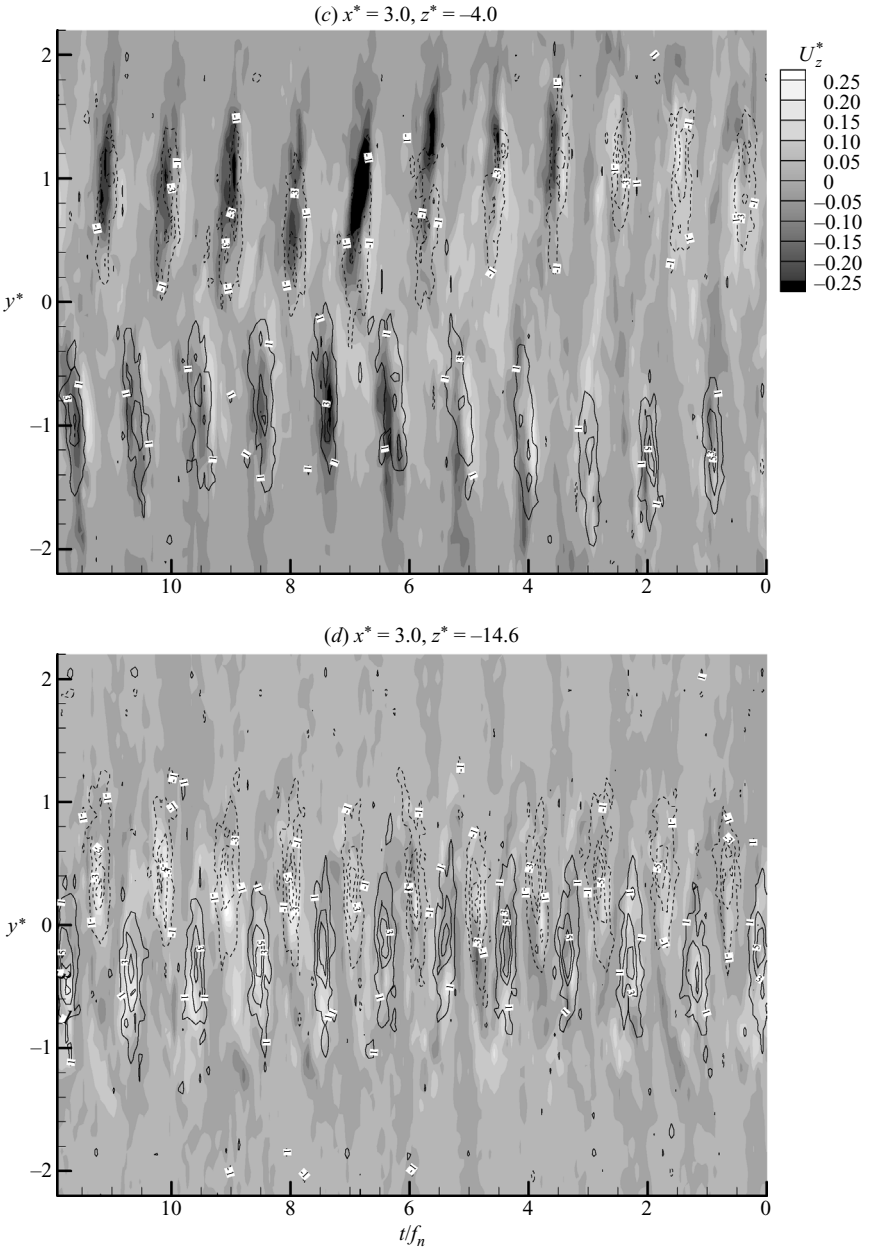

FIGURE 15. Space–time contour plots showing the correlation between vortex shedding and vertical flows for four different depths below the free surface. The ordinate is cross-stream position non-dimensionalized by cylinder diameter. Dimensionless time appears as the abscissa. Plots were obtained using vertical cross-stream DPIV measurements at $x/D = 3.0$ at four different depths: (*a*) $z/D = -1.0$; (*b*) $z/D = -2.0$; (*c*) $z/D = -4.0$; (*d*) $z/D = -14.6$. Note the variation and modulation in wake width along with direction and magnitude of vertical flows as a function of depth. Lines show contours of contant axial vorticity (solid, positive; dotted, negative).

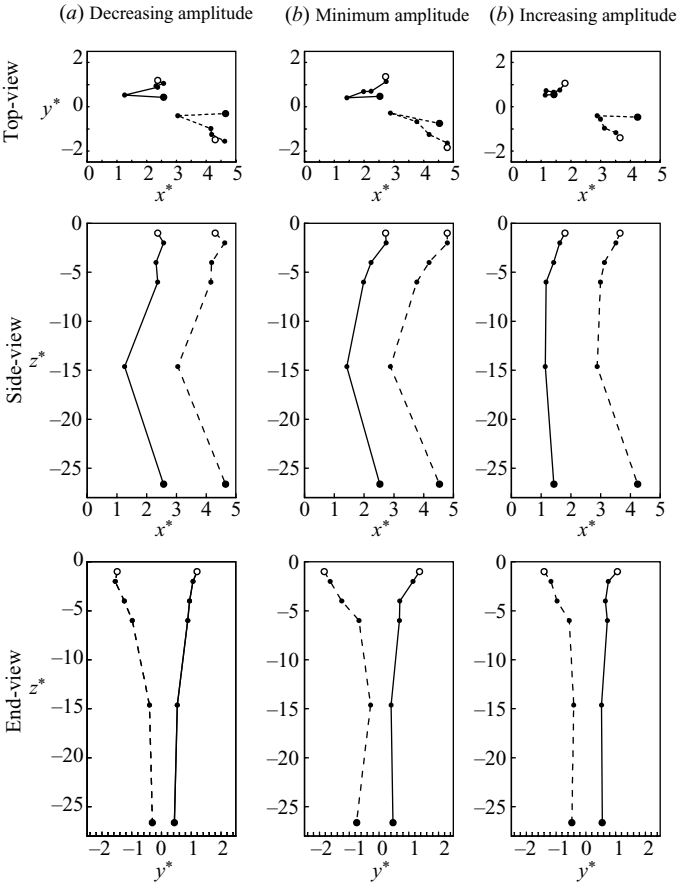

FIGURE 16. Orthographic projections of reconstructed phase-averaged vortex cores for a pair of Kármán vortices shed during (*a*) the decreasing portion of the cylinder beat cycle at $t^* = 1.24$; (*b*) the trough or minimum amplitude portion of the cylinder beat cycle at $t^* = 4.36$; (*c*) the increasing portion of the cylinder beat cycle at $t^* = 8.50$.

The results presented thus far clearly demonstrate the existence of axial flows with magnitudes in excess of 25% of U_∞. In addition, the vortices are significantly distorted close to the free-surface. To better visualize the effect of the free surface on the Kármán vortices, three-dimensional reconstruction of the vortex cores was done using the plan-view DPIV measurements. Vortices were tracked in six of the horizontal image planes at three different times in the phase-averaged beat cycle corresponding to decreasing amplitude, trough, and increasing amplitude. The vortex tracking algorithm was briefly described at the beginning of this section. The plane closest to the free-surface, $z/D = 0.5$, was not used.

For each frame, the geometric centres of a pair of opposite-sign vortices were located. Orthographic projections of the reconstructed Kármán vortices made for decreasing amplitude, trough, and increasing amplitude are shown in figures 16(*a*), 16(*b*), and 16(*c*), respectively. To facilitate interpretation of the reconstructed vortices, particularly for the top-view projections, the vortex centre measurement at $z/D = -1.0$ is identified by an open circle. The vortex measurement from the plane closest to the cylinder base, $z/D = -26.6$, is indicated by a solid black circle. Measurements in the

intermediate planes are not individually discriminated; they are shown as small black points. In each figure, the positive-sign (counter-clockwise) vortex, indicated with a dashed line, was shed before the negative-sign (clockwise) vortex, shown as a solid line.

There are a number of features of the three reconstructed vortices that are common to each of figures 16(*a*)–16(*c*). First, the wakes become wider on approaching the free-surface. This is clearly evident in the end-views of the three reconstructed vortices and is consistent with the space–time plots shown in figure 15. In addition, the portion of each Kármán vortex closest the bottom of the cylinder is ahead, i.e. downstream, of the vortex elements shed at the mid-height. This can be attributed to the longer formation length associated with small oscillation amplitudes. Finally, moving upward from the cylinder mid-height, $z/D = -14.6$ toward the free surface, the vortex leans downstream and away from the wake centreline. In brief, the most important similarity in figures 16(*a*)–16(*c*) is the high degree of curvature of the Kármán vortices, particularly close to the free surface.

It is the differences in curvature, however, which provide insight into the difference in vertical flows at different times in the oscillation beat cycle. This is particularly true in comparing vortex conformation for decreasing amplitude, figure 16(*a*), and increasing amplitude, figure 16(*c*). Compare, for example, the side-view projections. Observe that for the increasing amplitude case, figure 16(*c*), the Kármán vortices continue to lean forward on approaching the free surface. In contrast, for the decreasing amplitude case, figure 16(*a*), very close to the free surface, the vortices turn back downstream. Similarly, examination of the end-views in figures 16(*a*) and 16(*c*) indicates that for the decreasing amplitude portion of the beat cycle, the uppermost part of the Kármán vortices bends back toward the wake centreline, whereas the outward lateral spreading continues in the increasing amplitude case.

These differences in curvature close to the free surface provide insight into differences in vertical flows observed at different times in the cylinder beat cycle. If the vortex is leaning (as it clearly is), the circumferential flow around the vortex core will have a vertical component. Thus, as was seen in figure 15, there are places where up- and downflows may be found on either side of the vortex cores.

In addition, the degree of lateral spreading at the free surface will also have an effect on the axial pressure gradient within the vortex cores. As discussed in Hsu *et al.* (2000), free surfaces cause lateral spreading of near-surface turbulence and an attenuation of turbulent motions. Contour levels in figure 15 indicate that vorticity in the Kármán vortices may decrease very close to the free surface. This weakening would result in a reversal of the axial pressure gradient, causing near-surface fluid to be pumped downward away from the free surface. In summary then, the axial flows observed in the inverted pendulum cylinder experiment are due to a combination of axial pressure gradients and vortex curvature.

6. Conclusions

Vortex-induced vibration of a circular cylinder, mounted as an inverted pendulum, was investigated using two-colour flow visualization and DPIV measurement techniques. The response characteristics of the pendulum were observed to closely resemble those of elastically mounted cylinders with similar mass ratio and mass–damping. A particular focus of this work was the onset and disappearance of quasi-periodic beating of the cylinder in the upper branch or synchronization regime in the frequency–amplitude response. Detailed analysis revealed a ~ 0.1 Hz mismatch between the Kármán vortex shedding and cylinder oscillation frequencies. At the

same time, Kármán vortex strength modulates with time over the course of a phase-averaged beat period. Quasi-periodic beating, therefore, arises as a combination of frequency mismatch and modulated vortex strength. This beating behaviour naturally ends after a few beat periods because of physical constraints associated with the cylinder motion and vortex shedding.

The second focus of this study was the strong axial flows inside the Kármán vortices. These were observed to be in excess of 25% of the free-stream velocity. In general, the axial flows were toward the free surface in the direction of increasing cylinder amplitude. The axial flows can be attributed in part to the effect of linearly increasing oscillation amplitude along the span. Increased vortex strength with increasing amplitude creates an axial pressure gradient inside the vortex cores which pumps fluid toward the free-surface. Near the free surface, however, the axial flows were markedly different. There was an equal probability of upflow and downflow. Variations in upflow and downflow were correlated with the quasi-periodic beating of the cylinder amplitude; upflows occur during the increasing amplitude portion of the beat cycle while down flows occur during decreasing amplitude. The combined effects of the inverted pendulum motion and the free surface resulted in three-dimensional curvature of the Kármán vortices. The shape of the vortices also varied as a function of relative time within the cylinder beating cycle. It was hypothesized, in conclusion, that the effect of the free surface was to disrupt the axial pressure gradient which drove the primary up flow mechanism and also to induce lateral spreading/leaning of the top portions of the Kármán vortices. The combination of upflows and downflows close to the surface was probably a result of the fact that the Kármán vortices were not orthogonal to the free surface, except perhaps only at the free surface.

The authors would like to acknowledge the assistance of Mr John Petrowski in setting up the cylinder position sensor. Additionally, the authors would like to acknowledge the valuable suggestions provided by Professor Norman Zabusky particularly regarding the space–time analysis of the vertical motions. We also appreciate the assistance of Mr Shuang Zhang in computing the geometric centres of the Kármán vortices. Finally, support of the Office of Naval Research through Dr Thomas Swean is gratefully acknowledged.

REFERENCES

Atsavapranee, P., Benaroya, H. & Wei, T. 1999 Lock-in regimes and vortex shedding modes on a freely oscillating cylinder. *Presented at the ASCE Engng. Mech. Div. Conference, Baltimore, MD*.

Bearman, P. W. 1984 Vortex shedding from oscillating bluff bodies. *Annu. Rev. Fluid Mech.* **16**, 195–222.

Benaroya, H. & Wei, T. 2000 Hamilton's principle for external viscous fluid-structure interaction. *J. Sound Vib.* **238**, 113–145.

Bloor, M. S. 1964 The transition to turbulence in the wake of a circular cylinder. *J. Fluid Mech.* **19**, 290–304.

Chen, S. S. 1987 *Flow-induced Vibration of Circular Cylindrical Structures*. Hemisphere.

Dong, P. 2002 Phase averaged energy transport in the vortex-induced oscillation of a cylinder. PhD Dissertation; Dept. of Mech. & Aero. Engng, Rutgers, The State University, Piscataway, NJ.

Dong, P., Benaroya, H. & Wei, T. 2004 Integrating experiments into an energy-based reduced-order model for vortex-induced-vibrations of a cylinder mounted as an inverted pendulum. *J. Sound Vib.* **276**, 45–63.

Fujarra, A. L. C., Pesce, C. P., Flemming, F. & Williamson, C. H. K. 2001 Vortex–induced vibration of a flexible cantilever. *J. Fluids Struct.* **15**, 651–658.

GASTER, M. 1969 Vortex shedding from slender conaes at low Reynolds numbers. *J. Fluid Mech.* **38**, 565–576.

GASTER, M. 1971 Vortex shedding from circular cylinders at low Reynolds numbers. *J. Fluid Mech.* **46**, 749–756.

GREGA, L. M., HSU, T. Y. & WEI, T. 2002 Transport of streamwise vorticity in a corner formed by a solid wall and a free-surface. *J. Fluid Mech.* **465**, 331–352.

GREGA, L. M., WEI, T., LEIGHTON, R. I. & NEVES, J. C. 1995 Turbulent mixed boundary flow in the corner formed by a solid wall and a free-surface. *J. Fluid Mech.* **294**, 17–46.

HIRSA, A. & WILLMARTH, W. W. 1994 Measurements of vortex pair interaction with a clean or contaminated free-surface. *J. Fluid Mech.* **259**, 25–45.

HOVER, F. S., TECHET, A. H. & TRIANTAFYLLOU, M. S. 1998 Forces on oscillating uniform and tapered cylinders in a crossflow. *J. Fluid. Mech.* **363**, 97–114.

HSU, T. Y. 2000 Hydrodynamic stability at the exit of a papermachine headbox. PhD Dissertation Dept. of Mech. & Aero. Engng, Rutgers, The State University, Piscataway, NJ.

HSU, T. Y., GREGA, L. M., WEI, T., & LEIGHTON, R. I. 2000 Turbulent kinetic energy transport in a corner formed by a solid wall and a free-surface. *J. Fluid Mech.* **410**, 343–366.

KHALAK, A. & WILLIAMSON, C. H. K. 1999 Motions, forces and mode transitions in vortex-induced vibrations at low mass–damping. *J. Fluids Struct.* **13**, 813–851.

KITTAGAWA, T., FUJINO, Y. & KIMURA, K. 1999 Effect of free-end condition on end-cell-induced vibrations. *J. Fluids Struct.* **13**, 499–518.

LOGORY, L. M., HIRSA, A. & ANTHONY, D. G. 1996 Interaction of wake turbulence with a free-surface. *Phys. Fluids* **8**, 805–815.

SARPKAYA, T. & HENDERSON, D. 1985 Free surface scars and striations due to trailing vortices generated by a submerged lifting surface. *AIAA Paper* 85-0445.

SMITH, G. B. 1992 Collisional excitation of instabilities in impinging vortex rings. MS Thesis Dept. of Mech. & Aero. Engng, Rutgers, The State University, Piscataway, NJ.

TECHET, A. H., HOVER, F. S. & TRIANTAFYLLOU, M. S. 1998 Vortical patterns behind a tapered cylinder oscillating transversely to a uniform flow. *J. Fluid Mech.* **330**, 79–96.

TOMBAZIS, N. & BEARMAN, P. W. 1997 A study of three-dimensional aspects of vortex shedding from a bluff body with a mild geometric disturbance. *J. Fluid Mech.* **330**, 85–112.

VOORHEES, A. 2002 Three dimensional effects in the wake of a freely-oscillating inverted pendulum cylinder. *MS Thesis Dept. of Mech. & Aero. Engng, Rutgers, The State University, Piscataway, NJ.*

WALKER, D. T., LEIGHTON, R. I. & GARZA-RIOS, L. O. 1996 Shear-free turbulence near a flat free-surface. *J. Fluid Mech.* **320**, 19–51.

WANG, X. 1999 Visualizing tracking features in 3D time varying data sets. PhD Dissertation; Dept. of Mech. & Aero. Engg, Rutgers, The State University, Piscataway, NJ.

WARNCKE-LANG, A. & GHARIB, M. 2000 Experimental study of the wake behind a suface piercing cylinder for a clean and contaminated free–surface. *J. Fluid Mech.* **402**, 109–136.

WEI, T. & SMITH, C. R. 1986 The presence of secondary vortices in the wake of circular cylinders. *J. Fluid Mech.* **169**, 513–533.

WILLIAMSON, C. H. K. 1996*a* Vortex dynamics in the cylinder wake. *Annu. Rev. Fluid Mech.* **28**, 477–539.

WILLIAMSON, C. H. K. 1996*b* Three dimensional wake transition. *J. Fluid Mech.* **328**, 345–407.

WILLIAMSON, C. H. K. & ROSHKO, A. 1988 Vortex formation in the wake of an oscillating cylinder. *J. Fluids Struct.* **2**, 355–381.